Journal of Cluster Science (2021) 32:1107–1119
https://doi.org/10.1007/s10876-020-01869-6

ORIGINAL PAPER

Antimicrobial and Photocatalytic Degradation Activities of Chitosan-coated Magnetite Nanocomposite

Ahmed M. El-Khawaga[1] · Ayman A. Farrag[2] · Mohamed A. Elsayed[1] · Gharieb S. El-Sayyad[1,3] · Ahmed I. El-Batal[3]

Received: 9 March 2020 / Published online: 5 September 2020

Abstract

In this work, iron oxide nanoparticles (Fe_3O_4 NPs) were modified by chitosan (CS). Fe_3O_4 NPs were synthesized by co-precipitation method and their antimicrobial potential and photo-catalytic degradation of Chloramine T (CT) were investigated. The free Fe_3O_4 NPs and chitosan-coated Fe_3O_4 NPs (CS-Fe_3O_4 NPs) were characterized by XRD, FTIR, SEM, and HRTEM. Fe_3O_4 NPs have spherical shape and their diameter varied from 18.0 nm to 25.0 nm with average particle size at 21.0 nm. Antimicrobial activity was tested towards some pathogenic bacteria and *Candida* cells as zone of inhibition (ZOI) and minimum inhibitory concentration (MIC). UV-assisted photocatalytic degradation of CT was investigated. Various parameters affecting the photocatalytic efficiency such as (pH on CT removal, CT initial concentration, and adsorbent dose) were studied. Antimicrobial results showed that CS-Fe_3O_4 NPs possesses a maximum potential against *Escherichia coli*, *Bacillus subtilis* and *Candida albicans*, by 18.0, 17.0, 14.2 mm ZOI, respectively. Results obtained from the photocatalytic activity indicated that CS-Fe_3O_4 NPs (2.0 gm/l) possessed a promising removal potential, achieving 86.0% removal of CT in the neutral solution (pH = 7.0). The synthesized CS-Fe_3O_4 NPs are effective for the removal of CT and potent disinfectant agent for pathogenic microbes with possible application in the wastewater treatment.

Keywords Magnetite nanoparticles · Chitosan · Antimicrobial activity · Photocatalytic potential Reaction mechanism

Introduction

Nanotechnology has emerged as one of the most versatile fields in recent years [1, 2]. Nanoparticles (NPs) are drawing increasing attention due to their distinctive characteristics and minimal harmful effects [3, 4]. Magnetic NPs are becoming popular in bioengineering and biomedical applications [5, 6], due to their capability to act at the cellular and molecular level when exerted to in vitro and in vivo applications [7, 8]. Among NPs, iron oxide (Fe_3O_4) NPs are popular due to features such as super-paramagnetic, biocompatibility, crystalline structure, non-toxicity, monodispersity, water soluble, and cost-effective in the synthetic method [9, 10].

The crystalline morphology of Fe_3O_4 NPs consists of a high number of edges, corners and potentially-reactive sites which create an interest as potential antibacterial agents [11]. NPs with the size of less than 100 nm have consistent physical and chemical properties [12–14]. To make them suitable for bioengineering and biomedical applications they need to be coated to assure their without toxicity and stability in the biological medium [15, 16]. The surface coating agents may be enzymes, antibodies, proteins, drugs and polyelectrolytes to achieve better interactive properties on the surface of the synthesized NP [17].

The preferred process for the synthesis of Fe_3O_4 NPs is co-precipitation, because of its simplicity, and that it is

✉ Ahmed M. El-Khawaga
ahmedelkhwaga15@gmail.com

✉ Gharieb S. El-Sayyad
Gharieb.Elsayyad@eaea.org.eg

[1] Chemical Engineering Department, Military Technical College (MTC), Egyptian Armed Forces, Cairo, Egypt

[2] Botany and Microbiology Department, Faculty of Science (Boys), Al-Azhar University, Cairo, Egypt

[3] Drug Microbiology Lab, Drug Radiation Research Department, National Center for Radiation Research and Technology (NCRRT), Egyptian Atomic Energy Authority (EAEA), Cairo, Egypt

carried out under the mild condition without using any hazardous solvents. It has the potential for large-scale production, is cost effective and water soluble, all the necessary requirements for biomedical applications [18]. The crucial challenge in synthesis is to attain the optimum size and shape of the synthesized NPs, which is achieved by controlling pH, temperature, the nature of the salts, ionic strength and the insertion of the surface coating agents [19, 20]. Nanoparticles usually aggregate due to high surface energy and magnetisation [21, 22]. To avoid such aggregation, they are coated with a surface coating agent [23].

Chitosan, a biopolymer which is obtained from deacetylation of chitin, is a biocompatible, biodegradable, linear polysaccharide and consisting of three types of functional groups (amino, and primary and secondary hydroxyl groups) [24, 25]. These serve as an anchor for combining therapeutics, imaging agents and targeting ligands [18, 26]. Chitosan has antimicrobial activity against various microbes, and a negligible toxicity towards human cells [27].

Using standard microbiological methods [28, 29], we tested the antimicrobial properties of synthesised NPs on *Escherichia coli*, *Bacillus subtilis*, *Pseudomonas aeruginosa*, *Staphylococcus aureus* and *Candida albicans*; which responsible for infection Candidiasis, and forms a biofilm on the surface of the implantable biomedical devices [30]. *E. coli* is responsible for 80% of urinary tract infections (UTIs) [31–33]. Our objective was to synthesise chitosan-coated Fe_3O_4 NPs and evaluate their antimicrobial activity, and finally to explore the photocatalytic degradation of chloramine T (CT) from aqueous media. CT is an organic sodium salt derivative of toluene-4-sulfonamide with a chloro substituent in place of amino hydrogen. It must be noted that CT possesses chronic symptoms such as allergy, asthma and/or breathing problems if inhaled, additionally, it may cause critical skin burns and eye damage in low doses [34, 35]. Roorda et al. [36], reported the first case of an anaphylactic reaction caused by immediate-type hypersensitivity to CT. On review of the literature, we found several case reports describing urticaria, rhinitis and asthmatic bronchial obstruction caused by CT after skin contact or airborne exposure [37, 38].

Experimental Section

Chemicals and Reagents

Iron (III) chloride hexahydrate ($FeCl_3.\ 6H_2O$), iron (II) chloride tetrahydrate ($FeCl_2.\ 4H_2O$), sodium hydroxide (Na OH), chitosan $(C_6H_{11}NO_4)_n$ with deacetylation degree of 86 %, MW = 60 kDa, glacial acetic acid, cetyl trimethyl-ammonium bromide (CTAB), and chloramine T (CT) were purchased from E-Merck Products. All other reagents were analytical grade and directly-used without any purification.

Synthesis of Magnetite Nanoparticles (Fe_3O_4 Nps) by Co-precipitation Method

Aqueous solutions of Fe^{2+} and Fe^{3+} in their molar ratio (1: 2) are prepared in deionized water. Solutions are mixed in a separate flask and kept on ultrasonic stirrer for 10–15 min at room temperature to get homogenized solution. After that aqueous solution of Na OH (1 M) is added to the mixture of salt solutions drop wise at a fixed rate and elevated temperature (90 °C) on ultrasonic stirrer.

Co-precipitation occurs in alkaline medium between pH 8–14. Mixing and stirring continues till all salts are precipitated in black colour (formation of Fe_3O_4 NPs). Reaction is completed in two hours and further half an hour is required for aging. The black precipitate of magnetite NPs is separated by using external magnetic field and washed three times with deionized water till pH is near neutral (6.5). Finally, the magnetic Fe_3O_4 NPs were obtained after drying in a vacuum oven. The chemical reaction during the co-precipitation of ferrous and ferric salts occurs as follows (Eq. 1):

$$Fe^{2+} + Fe^{3+} + 8OH^- \cdots Fe_3O_4 + 4H_2O \quad (1)$$

In the present study instead of maintaining inert atmosphere to check the oxidation of ferrous ions (Fe^{2+}), co-precipitation was allowed at high temperature (80–90 °C).

Synthesis of Chitosan-coated Magnetite Nanoparticles (CS-Fe_3O_4 NPs)

The surface of magnetic Fe_3O_4 NPs was coated with a solution of CS for the purpose of obtaining modified Fe_3O_4 NPs. In a typical experiment, 0.25 g of magnetic Fe_3O_4 NPs was dispersed in a surfactant containing CTAB (2 g of CTAB dissolved in 400 ml of de-ionized water) (solution C) [39]. Then, 100 ml chitosan solution (0.02 g CS powders dissolved in 100 ml of 1% (w/v) acetic acid solution) was slowly-dropped into solution C. The mixture was continuously-stirred with a rotational speed of 1000 rpm for 1 hour at room temperature [39]. Then, CS coated by Fe_3O_4 NPs was magnetically-separated from solution by a magnet bar and thoroughly-washed several times with ethanol and deionized water. Finally, the obtained nanocomposites were dried overnight at 60 °C [39].

Characterization of Fe_3O_4 NPs and CS-Fe_3O_4 NPs

Powder X-ray diffraction (XRD) patterns were used to determine the crystal structures of the samples over a range of 20°–70°, using an XRD-6000 diffractometer (Shimadzu,

Tokyo, Japan) with Cu Kα radiation (λ 1.5406 Å) at 30 kV and 30 mA. Fourier transform infrared (FTIR) spectra of the materials were recorded over a range of 400–4,000 cm^{-1}, using a Nexus, Smart Orbit spectrometer (Thermo Fisher Scientific, Waltham, MA, USA) and the KBr disk method. The surface structure and homogeneity of the synthesized Fe_3O_4 NPs and CS-Fe_3O_4 NPs were characterized by scanning electron microscopy (SEM) ZEISS. The images of HRTEM were taken by a JEM-1010 (Jeol, Japan) operated at an accelerating voltage of 200 kV for determining the shape and size of the synthesized NPs.

Photocatalytic Degradation of Chloramine T (CT)

The photocatalytic degradation studies of the synthesized pure Fe_3O_4 NPs and chitosan functionalized Fe_3O_4 NPs (CS-Fe_3O_4 NPs) for removal of chloramine T (CT) were performed with batch equilibrium method [40]. A stock solution (100 mg/l) of CT was prepared by dissolving 0.1 g of CT powder in de-ionized water, and experimental solutions of desired CT concentrations were obtained by successive dilutions of the stock solution with de-ionized water.

(10 mg) of the prepared CS-Fe_3O_4 nanocomposite were added to (50 ml) of an aqueous solution of CT with initial concentration (C_o = 20 mg/L), under constant stirring at ambient temperature (24.0 ± 2 °C) for 30 min in dark, until adsorption–desorption equilibrium is attained between CT and the prepared photocatalyst (nanocomposite).

The used UV reactor was cylindrical shape having dimensions of 27 cm length, and 2.5 cm diameter and made up of stainless steel. The photo-reactor filled with 50 ml of contaminated solutions. The source of UV light is a 10 W high pressure mercury lamp (mean wavelength = 254 nm). At constant time intervals of irradiation, a syringe equipped with a filter (2.5 µm pore size) was used to draw out a sample of CT (3 ml).

The sample was then centrifuged for 10 min at 5000 rpm, to separate the photocatalyst. The degradation rate of CT was calculated by determining the variation in CT concentration verses irradiation time, by a UV–Vis. spectrophotometer (Agilent Technologies Cary 60 UV–Vis), at λ_{max} = 225 nm. De-ionized water was used as a reference [40].

Antimicrobial Activity of Fe_3O_4 NPs and CS-Fe_3O_4 NPs

The synthesized chitosan coated magnetic Fe_3O_4 NPs (CS-Fe_3O_4 NPs; 10.0 µg/ml) were tested for their antimicrobial performance after conducting the agar-disc distribution process [41–44]. All samples were examined upon several isolates of pathogenic bacteria-causing urinary tract infection (UTI) which received from the culture collections in Drug Microbiology Lab., Drug Radiation Research Dep., NCRRT, Cairo, Egypt. Bacterial strains were *E. coli, S. aureus, B. subtilis, P. aeroginosa* and *Candida albicans.* The bacterial inoculums were fixed at 0.5 McFarland (1–3) × 10^8 CFU/ml, at a fixed 600 nm UV–Vis. spectrophotometer [45, 46]. The growth inhibition of all the investigated bacterial and yeast strains was estimated by the zone of inhibition (ZOI) after 24 hours incubation [42, 46]. Standard antibiotic discs Gentamycin (CN) at conc. 10 µg/ml and Nystatin (NS) at concentration 100 µg/ml with 6.0 mm diameter were chosen to determine the performance of the considered magnetic Fe_3O_4 NPs and CS-Fe_3O_4 NPs.

The serial dilutions method of Luria–Bertani (LB) medium was applied to determine the minimum inhibitory concentrations (MIC) of the tested CS-Fe_3O_4 NPs and Fe_3O_4 NPs [43, 47]. For these determinations, a negative control such as the medium broth, positive control such as the examined pathogenic microbes and the used medium broth and CS-Fe_3O_4 NPs and Fe_3O_4 NPs (beginning with concentration = 20.0 µg/ml) were applied. MIC was determined next 24 hours of incubation at 36.0 ± 1.0 °C [48, 49].

The inoculums were fixed as mentioned-before in the first antimicrobial screening [45, 49]. MIC was defined by using the ELISA plate method after setting the fixed wavelength at 600 nm [48, 50]. The MIC was described as the lowest concentration of CS-Fe_3O_4 NPs and Fe_3O_4 NPs that inhibits 99.0% of the growth of the tested bacteria and yeast cells.

Statistical Analysis

The mathematical analysis of the effects was conducted by applying the ONE WAY ANOVA (at $P < 0.05$), the least significant differences (LSD), and Duncan's multiple systems [51]. The effects and data were examined and decided through SPSS software (version 15).

Results and Discussion

Characterization of the Prepared Fe_3O_4 NPs and CS-Fe_3O_4 NPs

X-Ray Diffraction

Figure 1 shows the results of x-ray diffraction (XRD) analysis for magnetic Fe_3O_4 NPs and CS-Fe_3O_4 NPs synthesized by co-precipitation method. The Fe_3O_4 diffraction patterns have six main peaks at 2θ values of 30.1°, 35.5°, 43.2°, 53.5°, 57°, and 62.8° which corresponding to the

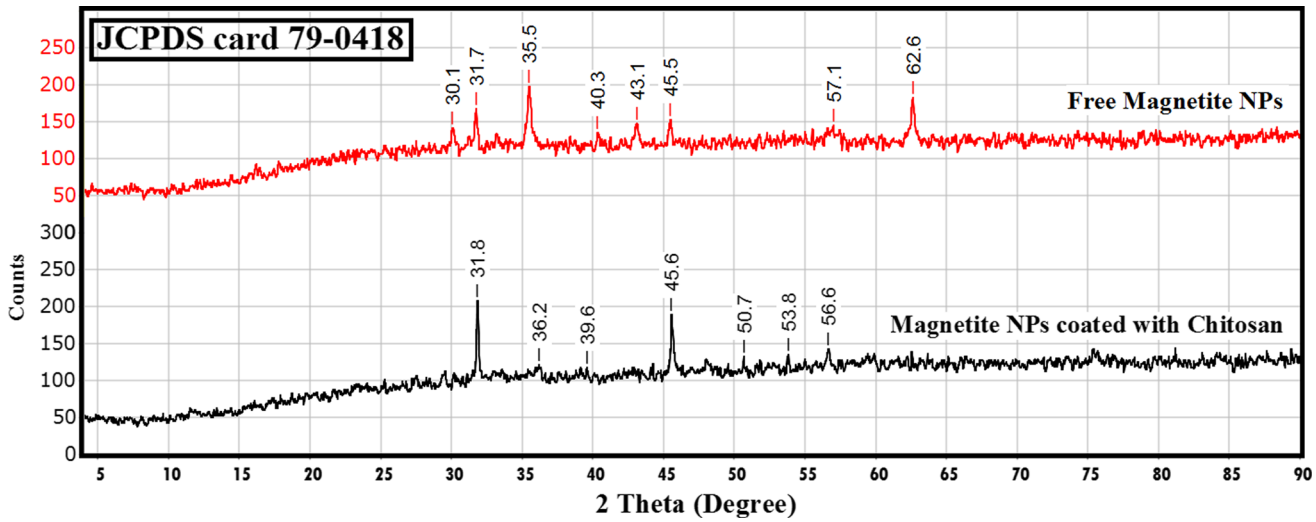

Fig. 1 XRD patterns of free magnetite NPs and magnetite NPs coated with chitosan

reflection from (220), (311), (400), (422), (511), and (440) crystal planes, respectively. Positions and relative intensities of all the peaks are in accordance with the cubic crystalline system of Fe_3O_4 NPs. Patterns of iron oxides and oxy-hydroxide products of the JCPDS card 79–0418 database were included for comparison [52].

The narrow shape peaks of materials indicate that the synthesized NPs have relatively-high crystallinity, and without the appearance of the impurities phase of goethite α-FeO (OH) and hematite (Fe_2O_3) corresponding to the diffraction peaks of (110), (104) at 2θ positions of 21.22° and 33.15°.

Broadness of the diffraction peaks was related to particle sizes. Scherer's equation was used to calculate the average particle size D.

$$D = k\lambda/(\beta\cos\theta) \quad (2)$$

In this equation, θ is the angle of the peak, β is the full width at half maximum (FWHM) of the respective XRD peak, λ is the x-ray radiation wave-length in angstroms, and k is a constant. The broadening of Bragg's peaks indicates the formation of NPs. The calculated mean crystallite size of the synthesized Fe_3O_4 NPs was about 23.0 nm.

FTIR Spectra Analysis

FTIR was performed to confirm the functional groups on the surface of the synthetic materials. The spectra of pure Fe_3O_4 NPs and CS-Fe_3O_4 NPs were shown in Fig. 2. The presence of two strong peaks of Fe_3O_4 NPs and CS-Fe_3O_4 NPs at 628.1 and 573.4 cm^{-1}, respectively shows the formation of magnetic NP. Moreover, the band at 573.4 cm^{-1} was confirmed as the Fe–O stretching vibration of tetrahedral sites of spinel structure [18]. The noted peak at

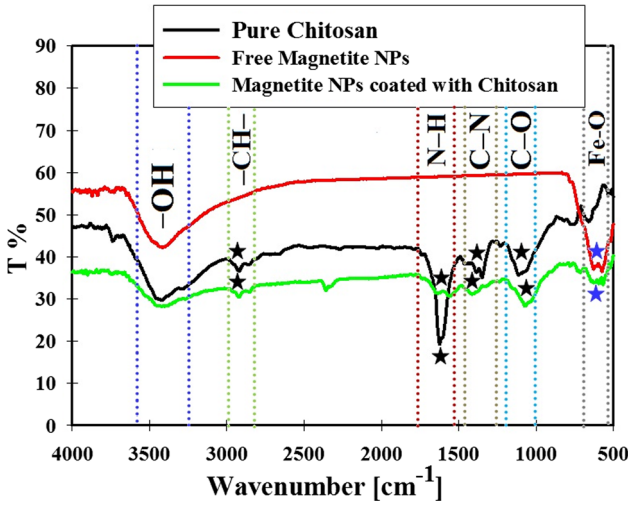

Fig. 2 FTIR spectrum of free magnetite NPs, pure chitosan and magnetite NPs coated with chitosan where, black stars represented the presence of functional groups in both pure chitosan, and magnetite NPs coated with chitosan, and blue stars exhibited the presence of functional groups in both free magnetite NPs, and magnetite NPs coated with chitosan

467.7 cm^{-1}, attributed to the tetrahedral and octahedral sites [53], peak at 3415 cm^{-1} was due to the O–H stretching model adsorbed on the surface of the Fe_3O_4 NPs [54]. In the case of CS coated magnetic Fe_3O_4 NPs, the coating of CS is established by the appearance of the peak at 2923 cm^{-1} considered to be the stretching vibrations of –CH– in chitosan. The peak at 1634 cm^{-1} is relevant to the N–H vibration for the chitosan. In addition, the C-N vibration of amino group is at 1416 cm^{-1} and the C–O in the ether group is at 1071 cm^{-1}.

Scanning Electron Microscopy (SEM) and Transmission Electron Microscopy (TEM) Analysis

Morphological analysis was studied with electron microscopic images. In the SEM images of Fe_3O_4 NPs, it can be clearly-seen that the particles are uniformly-aggregated, spherical shaped with a grain size 8–25 nm (Fig. 3). SEM images of magnetic uncoated-Fe_3O_4 NPs and CS-Fe_3O_4 NPs are shown in Fig. 3. The results suggested that all NPs are most spherical in shape and the grain size of CS-Fe_3O_4NPs was in the range from 8.0 to 17.0 nm.

From these results, it may indirectly-prove that the magnetic core/shell particles remain single crystals to have an average diameter of 8.0 nm, and (chitosan) shells have the approximate thickness of 9.0 nm. The results suggest that the (chitosan) layer is uniformly-deposited on Fe_3O_4 NPs, as shown in Fig. 3b.

On the other hand, the TEM images (Fig. 4) of free Fe_3O_4NPs and CS-Fe_3O_4NPs reveal that the magnetite NPs are spherical in shape, and the size was ranged from 18.0 nm to 25.0 nm and the average particle size was determined to be 21.0 nm. Also, the immobilized chitosan on Fe_3O_4 NPs did not lead to the aggregation between the particles and the size did not change. It was concluded that all the chitosan in the final product is chemically-bound (covalent bond) to the Fe_3O_4 NPs. FTIR spectrum results (Fig. 2) demonstrated that, the precipitation reactions carried out with chitosan rendered Fe_3O_4 NPs coated by this polymer.

In Vitro Antimicrobial Activity of Free Magnetite NPs and Magnetite NPs Coated with Chitosan

It is remarked from the disc agar distribution method (as a screening procedure) that the CS- Fe_3O_4 NPs and Fe_3O_4 NPs represented a qualitative antimicrobial potential toward all the tested bacteria and *Candida* pathogens. The *in-vitro* ZOI result verified that CS-Fe_3O_4 NPs exhibited its encouraged antibacterial activity against *E. coli* (18.0 mm ZOI; Fig. 5a), and *B. subtilis* (17.0 mm ZOI; Fig. 5b) as displayed in Table 1.

It worth considering that the antibacterial potency of CS-Fe_3O_4 NPs was significantly more powerful than Fe_3O_4 NPs, CS and standard antibacterial agents (Gentamycin; CN).

From our results, the synthesized CS-Fe_3O_4 NPs show a broad-spectrum antimicrobial activity, but it more active against Gram-negative bacteria more than Gram-positive bacteria.

The activity towards Gram-negative bacteria due to its potential on the cell wall, since it is composed of multi-thin layers of lipopolysaccharide, lipid, and peptidoglycan, while Gram-positive was resistant to the synthesized CS-Fe_3O_4 NPs due to its cell wall compact structure (solid peptidoglycan layers) [55].

Additionally, the incorporated CS-Fe_3O_4 NPs were promising antifungal factors, they exhibited tremendous antifungal efficiency upon *C. albicans* (14.2 mm ZOI; Fig. 5c) as recorded in Table 1.

In our study, there is a relationship between the characteristics of the incorporated CS-Fe_3O_4 NPs and the antimicrobial effects since, the crystal size of the synthesized CS-Fe_3O_4 NPs was small (15.0 nm; Fig. 1), dispersed, spherical form with particle size in the nano-scale (21.0 nm; Fig. 4b), and highly-distributed NPs (Fig. 3a) which served as an essential objective in enhancing the antimicrobial potency of CS-Fe_3O_4 NPs at low concentration (10.0 µg/ml), against all the examined bacteria and *Candida* sp.

They reported individual physical and chemical properties more than traditional organic and artificial antimicrobial agents such as the decreased crystal sizes and reduced average particle size, more stability and a higher potency for interaction with more further pathogenic

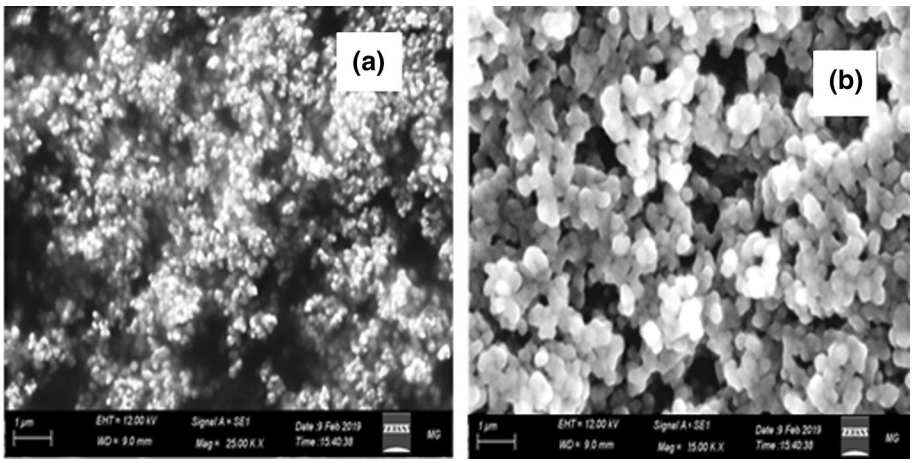

Fig. 3 Surface and morphological characteristics of (a) free magnetite NPs, and (b) magnetite NPs coated with chitosan using SEM technique

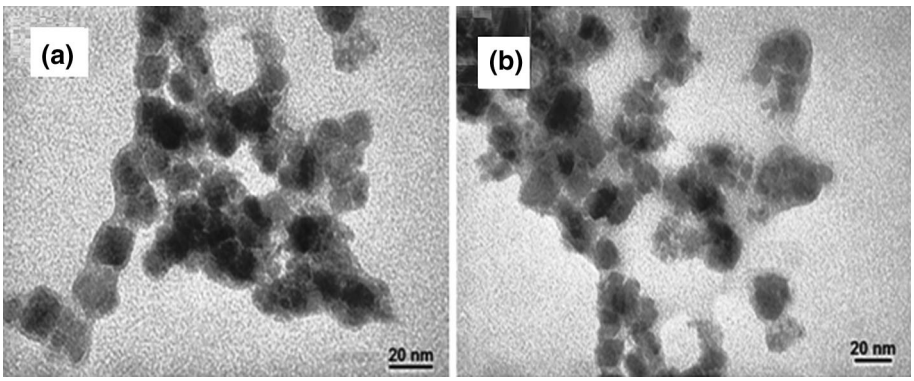

Fig. 4 Shape and average particle size determination of (a) free magnetite NPs, and (b) magnetite NPs coated with chitosan using TEM technique

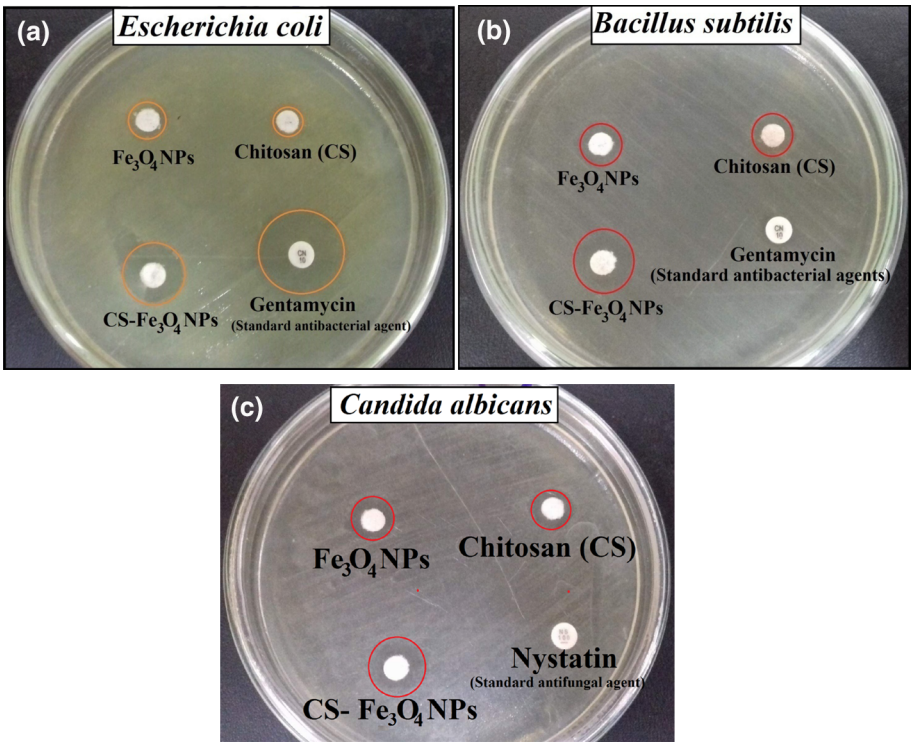

Fig. 5 Antimicrobial activity of CS-Fe_3O_4 NPs, Fe_3O_4 NPs and Chitosan (CS) against multi-drug resistant (MDR) bacteria, and pathogenic *Candida* species measured as ZOI (mm): where (a) *Escherichia coli*, (b) *Bacillus subtilis,* and (c) *Candida albicans*

bacteria and *Candida* sp., consequently, increasing their antimicrobial potential [56–58].

The MIC results of CS-Fe_3O_4 NPs against all the tested pathogenic bacteria and *Candida* sp. were in the range from 10.0 to 0.625 µg/ml as mentioned in Table 1. CS-Fe_3O_4 NPs possess promising MIC of 0.625 µg/ml against *E. coli* and *B. subtilis*.

CS-Fe_3O_4 NPs size was not simply parameter indicating the antimicrobial characteristics, but other features such as mono-dispersity, simplicity, stability, and the appearance should be considered [58, 59].

The antimicrobial mechanism of the synthesized magnetite NPs needs to be explained in details. There were remarkably suggested mechanisms such as Reactive Oxygen Species (ROS) production ($^{\cdot}O_2^-$ and $^{\cdot}OH$) which depends upon the crystallite size and larger surface area as explained in Fig. 6 [60, 61].

The production of ROS begins when the prepared magnetite NPs within the bacterial cell in the presence of light, which starts to the excitation of the electrons from the valence band to the covalent band with a new energy level which exit h^+ in the valence band. Positively, that reaction mechanism explains the band gap effect on the antimicrobial activity [62]. The generated ROS causing serious damage effect when combined with the biological macromolecules inside the bacterial cell such as DNA, lipids, proteins, and carbohydrates (Fig. 6) [63].

El-Batal et al., [64] have claimed that there are four mechanisms interpret the action of metal NPs on the microbial pathogens. They found that Fe metal in

Table 1 Antimicrobial activities of CS-Fe_3O_4 NPs, Fe_3O_4 NPs and Chitosan (CS) against multi-drug resistant (MDR) bacteria, and pathogenic *Candida species* measured as ZOI (mm) and MIC (μg/ml)

Pathogenic microbes	ZOI of CS-Fe_3O_4 NPs (10.0 μg/ml) (mm)	MIC of CS-Fe_3O_4 NPs (μg/ml)	ZOI of Fe_3O_4 NPs (10.0 μg/ml) (mm)	MIC of Fe_3O_4 NPs (μg/ml)	ZOI of CS (mm)	CN or NS
Escherichia coli	$18.0^{e} \pm 0.5$	0.625	$10.0^{d} \pm 0.3$	5.0	$8.5^{a} \pm 0.3$	$22.0^{a} \pm 0.3$
Pseudomonas aeruginosa	$11.0^{b} \pm 0.3$	2.5	$8.5^{b} \pm 0.4$	10.0	Nil	Nil
Staphylococcus aureus	$10.0^{a} \pm 0.5$	2.5	$8.0^{a} \pm 0.4$	10.0	Nil	Nil
Bacillus subtilus	$17.0^{d} \pm 0.3$	0.625	$10.5^{c} \pm 0.4$	5.0	$9.5^{b} \pm 0.2$	Nil
Candida albicans	$14.2^{c} \pm 0.4$	1.25	$10.5^{c} \pm 0.4$	5.0	$9.0^{b} \pm 0.3$	Nil
LSD	1.2	–	0.9	–	2.2	7.9

Values are presented as means ± SD (n = 3). Data within the groups were analyzed using one-way analysis of variance(ANOVA) followed by $^{a, b, c, d, e}$ Duncan's multiple range test (DMRT)

Nil means that, no ZOIs had been measured

LSD = Least Significant Difference, CN = Gentamycin; 20 μg/ml (standard antibacterial agent). NS = Nystatin (standard antifungal agent)

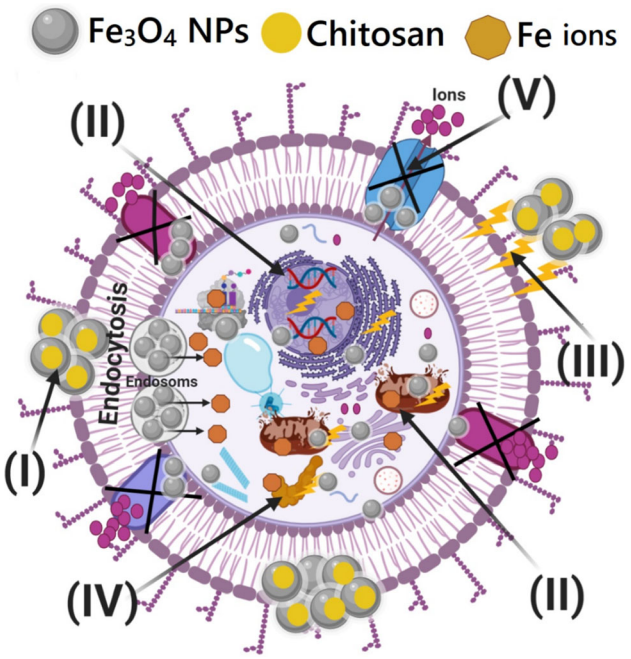

Fig. 6 Schematic representation regarding the five prominent ways of antimicrobial potential of CS-Fe_3O_4 NPs, where (I) CS-Fe_3O_4 NPs adhere to the microbial cell surface and results in membrane damage and altered transport activity; the role of chitosan is to permit the interaction between positively-charged functional group (-NH_3^+) and negatively-charged bacterial cell, (II) Fe_3O_4 NPs penetrate inside the microbial cells and interact with cellular organelles and biomolecules, and thereby, affect respective cellular machinery, (III) Fe_3O_4 NPs create and increase the ROS inside the microbial cells leading to cell damage, (IV) Fe_3O_4 NPs modulate the cellular signal system and causing cell death, and (V) Fe_3O_4 NPs block the ions transport from and to the microbial cell. Fe_3O_4 NPs may serve as a vehicle to effectively-deliver Fe ions to the microbial cytoplasm and membrane, where proton motive force would decrease the pH to be less than 3.0 and therefore improve the release of Fe ions

magnetite nanosrtucture is started by the adhesion across the surface of the bacterial cell wall and layers (Fig. 6).

After that, they deal with the understanding of nano-metals Fe inside the bacterial cell and cleavage all of the intracellular molecules like biological molecules. Then, the cellular toxicity (oxidative stress) created by the formation of ROS has happened (Fig. 6).

Finally, nano-metals (Fe) were affected against signal transduction pathways. Furthermore, the antibacterial potential of magnetite nanostructure may be due to the interaction with a specific enzyme (that catalyzes mannose-6-phosphate exchange to fructose-6-phosphate) by altering its configuration and subsequent its activity as displayed in Fig. 6. Fructose-6-phosphate is an essential compound in the glycolysis pathway which is connected to the carbo-hydrate catabolism in all microbes [35].

Photocatalytic Degradation of Chloramine T (CT) Using Magnetite NPs Coated with Chitosan

The photocatalytic activity of the synthesized chitosan coated Fe_3O_4 nanocomposite was determined using the photocatalytic degradation of CT solution under UV irra-diation. Figure 7 illustrates the absorption decline with irradiation time through the photocatalytic degradation of CT solution by (10 mg) of the prepared nanocomposite against (CT) solution (50 ml; 20 mg/L). Upon increasing the irradiation time, the strong absorption bands of CT recorded at 225 nm (indicating the maximum wavelength λ_{max} for the CT) have been continuously-reduced. Absor-bance of CT solution was reduced by 86 % after 60 min of UV irradiation at the specified experimental conditions.

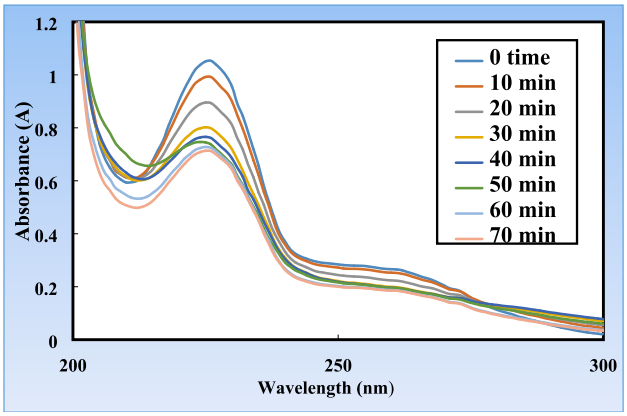

Fig. 7 UV spectra of chloramine T showing its degradation with time (10 mg of the nanocomposite, 50 ml (CT) solution (20 ppm), Temp., = 25 °C and pH = 7)

Effect of Initial Concentration of CT on Degradation Efficiency

As the initial CT concentration plays a vital role in the photocatalytic degradation process, the effect of ionic strength of CT was studied by varying the initial concentration of CT and keeping other reaction conditions unaltered. Figure 8 represents the variation of degradation capacity as a function of contact time at different initial CT concentration (10, 20, and 30 mg/l). At higher concentration of CT, the degradation capacity was recorded to be high. The higher degradation capacity at higher CT concentration is because of stronger interaction with the nanocomposite at higher ionic concentration of CT.

Effect of pH on Degradation of CT

For photocatalytic degradation studies, one of the vital factors is its dependence on pH of the solution. The effect of initial pH values of CT solution was studied for 90 min of specified experimental conditions (10 mg of the prepared nanocomposite, 50 ml of 20 mg/L CT solution, Temp., = 25 °C). A plot showing the variation of CT removal (%) with time at different solution pH (5.0, 7.0 and 9.0) is exhibited in Fig. 9a. The maximum CT degradation (%) ~ 86.0% in equilibrium was observed at pH 7.0, while, pH 5 and 9 showed degradation efficiencies of 75.5% and 71.5%, respectively. Hence, all the further photocatalytic degradation experiments were conducted at pH 7.0 in this study.

To determine the point of zero charge (PZC) of the CS-Fe_3O_4 nanocomposite, 0.01 g (CS-Fe_3O_4 NPs) was added to 50 mL (0.01 M NaCl solution). The pH values of the solutions were adjusted with HCl or Na OH to be as 2, 4, 6, 8, 10, and 12. The samples were stirred at 200 rpm for 48 h. The pH values of the solutions were measured after magnetically-separation of (CS-Fe_3O_4 NPs). The pH of the PZC value was determined by using a plot which shows the final pH versus initial pH. These results are presented in Fig. 9b.

According to Fig. 9b, the pH of the PZC occurred where there is no significant difference between final and initial

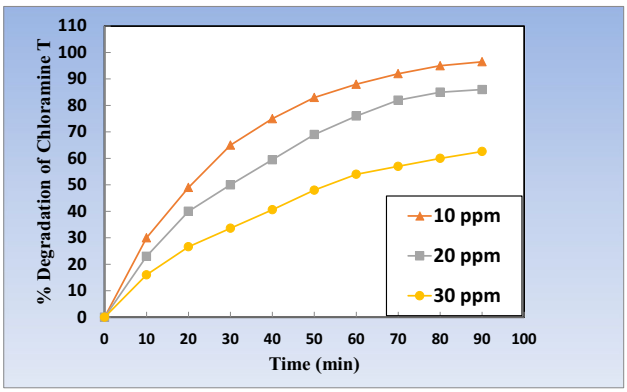

Fig. 8 Effect of initial concentration of CT solution on the degradation efficiency (10 mg of composite, 50 ml (CT) solution, Temp., = 25 °C and pH = 7)

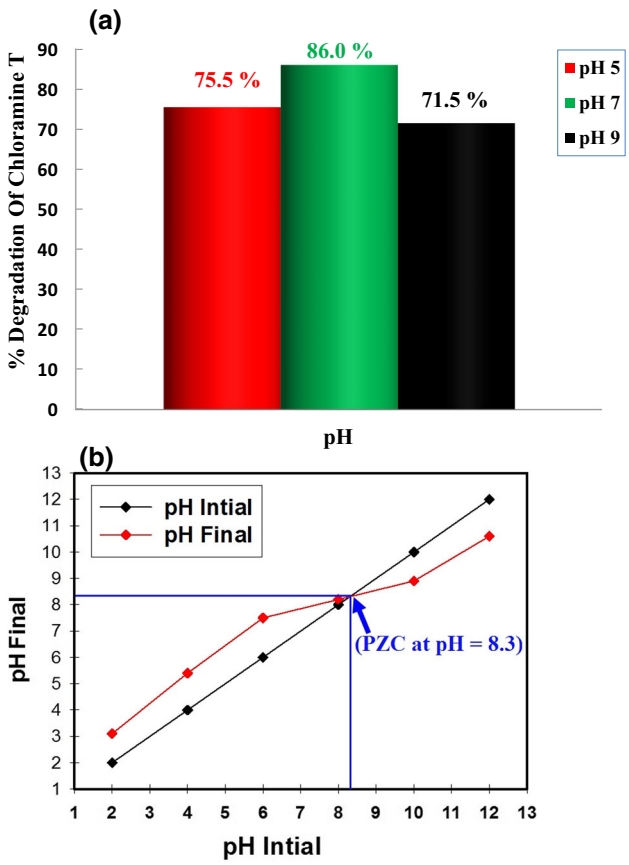

Fig. 9 **a** Influence of initial pH on the chloramine T removal (20 mg/L CT (50 ml), 10 mg nanocomposite and 90 min irradiation time). **b** The point of zero charge (PZC) of CS-Fe_3O_4 NPs at different pH values

pH values, and was determined to be at pH = 8.3. It means that the surface charge of the photocatalyst (CS-Fe_3O_4 NPs) is positive and negative when pH < pH of PZC and pH > pH PZC, respectively. Besides, when the pH of the solution is equivalent to the pH of the PZC, the photocatalyst surface charge is neutral and the electrostatic force between the photocatalyst surface and ions (CT ions) is negligible [65].

According to the pH of the PZC value, the pH of the PZC regarding CS-Fe_3O_4 NPs was 8.3, and this result was explained why the photocatalytic degradation of CT was maximum at pH 7.0 as displayed in Fig. 9a. Hence at this point the net surface charge of the CS-Fe_3O_4 NPs is positive which attracted with the negative charge of CT and improve the photocatalytic degradation of CT.

The photocatalytic degradation of CT began to decrease at pH = 9.0 this occur due to at this point the net surface charge of the CS-Fe_3O_4 NPs is negative and the repulsion forces between the negative charge of CT and net surface charge of the CS-Fe_3O_4 nanocomposite which is negative at pH = 9.0. The reason which make the photocatalytic degradation decreases at pH 5.0 unexpectedly is at highly acidic medium the metal oxide leaching may be occur which decrease the catalyst concentration [65]. On the other hand, chitosan contains reactive amino group ($–NH_2$), which is easily protonated to form ($-NH_3^+$) in acidic solutions (pH 5.0). The high adsorption capacity is due to the strong electrostatic interaction between the NH_3^+ of chitosan and negative charge of CT [66], which explains the higher catalytic performance in pH 5 (75.5%) more than the catalytic potential at pH 9 (71.5%).

Effect of the Photocatalyst's Dose on Degradation Efficiency

The effect of nanocomposite dose on the photocatalytic degradation process was studied by keeping other parameters such as initial CT concentration, pH of the solution, and temperature fixed. Figure 10 depicts the effect of photocatalyst dose on CT degradation process, where the dose amount of CS-Fe_3O_4 NPs was varied (0.1, 0.2 and 0.4) g/L. During this study, the initial concentration of CT was kept constant at 20 mg/l and the pH of the system was kept at 7.0 at 25 °C. It was observed that the percentage degradation of CT significantly-depends on the photocatalyst dose and increases with increasing dose. This direct-proportional between the degradation efficiency and the dose of reaction medium's photocatalyst can be attributed to the increase in the active sites and large surface area available for CT degradation [67]. From the Fig. 10, it is noticed that percentage degradation of CT approaches nearing 86% at a dose of 2 g/L with the above-mentioned experimental condition.

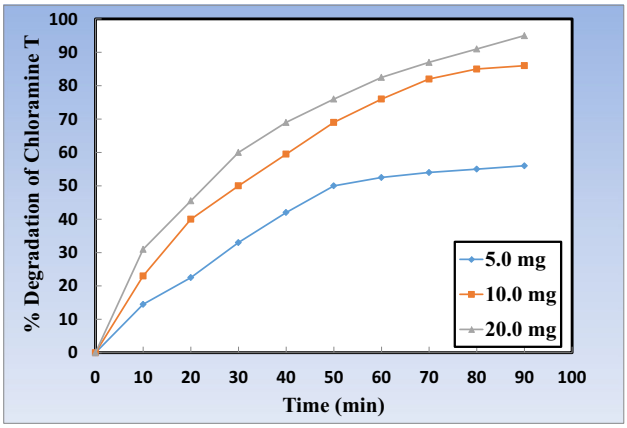

Fig. 10 Effect of the photocatalyst dose on CT degradation efficiency (50 ml (CT) solution (20 mg/L), Temp., = 25 °C and pH = 7)

Kinetic Studies

The degradation rate of CT can be calculated by the following Eq. (3):

$$-\ln C_t/C_O = -Kt \tag{3}$$

where C_t and C_o are the remaining and the initial concentrations of Chloramine T, respectively, while (t) is the irradiation time and (k) represent the degradation rate constant.

Figure 11a shows a relation of -ln C_t/C_0 vs. time. The results shown that, the kinetics of the degradation reaction followed first-order rate laws ($R^2 > 98$) at initial concentrations.

Moreover, as revealed from Fig. 11b, there is an inverse relation between the apparent first order rate constants and CT initial concentration. This recorded dependence of reaction rate constants on initial concentration is in a good agreement with literature [57, 58, 68].

The proposed reaction mechanism regarding the interaction between the prepared CS-Fe_3O_4 NPs and CT is shown in Fig. 12, according to our recent published papers [69, 70]. After UV-light excitation of Fe_3O_4 layer, charge carriers will be photogenerated and redox reactions will be initiated [58]. Then, the generated free radicals (such as $OH^{\cdot}$ And $O_2^{\cdot -}$) will degrade CT into two potential products, p-touluene sulfonamide and hypochlorites that can be easily dissociated into O_2 and Cl^- ions as shown in Fig. 12. Additionally, the role of CS can be mentioned as they were contains reactive amino group ($–NH_2$), which is easily protonated to form $-NH_3^+$, in acidic solutions (pH 5.0). The high adsorption capacity is due to the strong electrostatic interaction between the NH_3^+ of chitosan and negative charge of CT, as displayed in Fig. 12 [66].

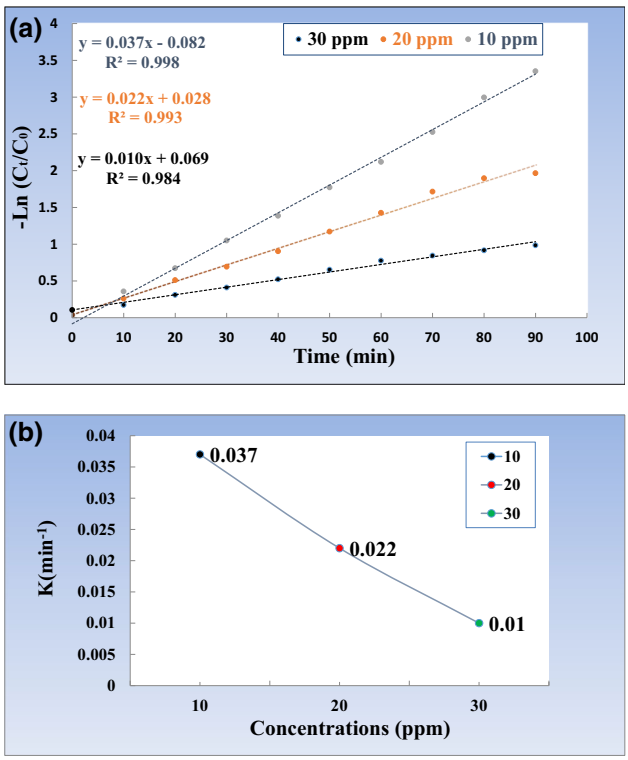

Fig. 11 **a** The first order kinetics of chloramine T degradation (10 mg of composite, 50 ml (CT) solution, Temp., = 25 °C and pH = 7). **b** Apparent first order rate constants vs. CT's initial concentration

Conclusion

Fe_3O_4 NPs have been synthesized by a chemical co-precipitation method and characterized by structural and optical tools. The surface of Fe_3O_4 NPs was stabilized with chitosan (CS) by a direct addition method to obtain modified CS-Fe_3O_4 NPs. Furthermore, their antimicrobial behavior has been examined against different pathogenic bacteria and yeast which separated from urine samples of UTI-patients. The photocatalytic efficiency of the prepared CS-Fe_3O_4 NPs was tested against chloramines T (CT). Also, various parameters affecting the efficiency of removal potential such as (pH on adsorption of CT, CT initial concentration, and adsorbent dose) have been studied. Based on XRD, TEM and SEM analyses, it is found that CS-Fe_3O_4NPs are located at the core, while the CS are coated this core, producing CS-functionalized Fe_3O_4 NPs with particle size varies from 18.0 nm to 25.0 nm with average particle size at 21.0 nm. The surface behavior reveals in homogeneous grain appearance with remarkable smooth agglomerates can be observed due to the occupation of a large quantity of CS at the grain boundary which could control the grain growth. From FTIR results, the presence of two strong peaks of all materials at 628.1 cm^{-1} and 573.4 cm^{-1} shows the formation of magnetic NPs. Moreover, the noted peak at 573.4 cm^{-1} was confirmed as the Fe–O stretching vibration of tetrahedral sites of spinel structure. The *in-vitro* ZOI and MIC result verified that CS-functionalized Fe_3O_4 NPs exhibited its encouraged antimicrobial activity against *E. coli* (18.0 mm ZOI and 0.625 µg/ml MIC), *B. subtilis* (17.0 mm ZOI and 0.625 µg/ml MIC), and *C. albicans* (14.2 mm ZOI and 1.25 µg/ml MIC). So, there is no toxicity regarding the use of CS-Fe_3O_4 NPs in the different fields. It should be noted that CS-Fe_3O_4 NPs are also active upon Gram-negative than Gram-positive bacteria. Results obtained from the photodegradation activity indicated that chitosan-coated Fe_3O_4 NPs (5.0 gm/l) was a promising removal factor achieving 86.0% CT removal in a neutral solution (pH = 7.0). The synthesized CS-Fe_3O_4NPs are promising for potential applications in industry, food processing and packaging, pharmaceutical uses, wastewater treatment and cosmetics.

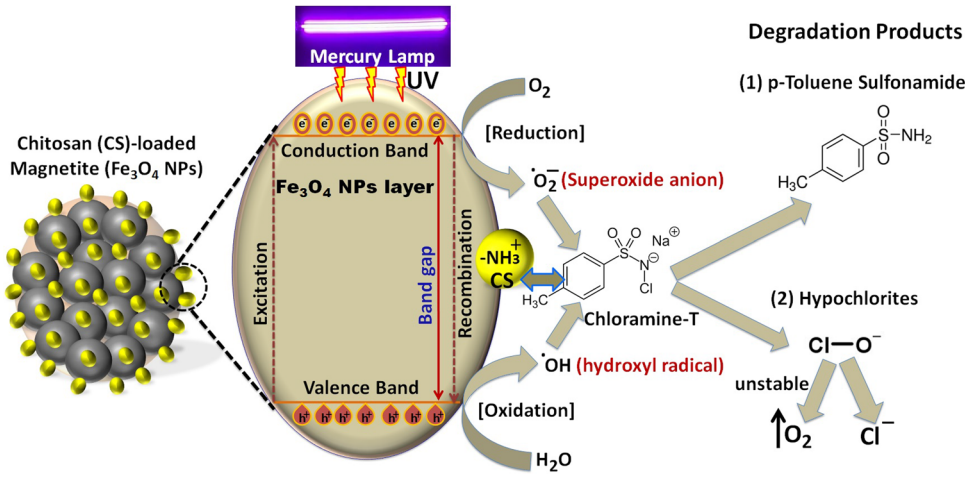

Fig. 12 Proposed mechanism of photocatalytic degradation of chloramines T (CT) with the prepared CS-Fe_3O_4 nanocomposite

Ethical approval:

Not applicable.

Acknowledgments The authors would like to thank the Nanotechnology Research Unit (P.I. Prof. Dr. Ahmed I. El-Batal), Drug Microbiology Lab., Drug Radiation Research Department, NCRRT, Egypt, for financing and supporting this study under the project "Nutraceuticals and Functional Foods Production by using Nano/Biotechnological and Irradiation Processes". Figures 6 and 12 in this paper were created with BioRender.com.

Funding Not applicable.

Compliance with Ethical Standards

Conflict of interest The authors declare that they have no conflict of interest.

Research Involving Human Participation and/or Animals Not applicable.

Informed Consent Not applicable.

References

1. Patra, J.K., et al., *Nano based drug delivery systems: recent developments and future prospects.* Journal of nanobiotechnology, 2018. 16(1): p. 71.
2. El-Batal, A., et al., *Synthesis of silver nanoparticles and incorporation with certain antibiotic using gamma irradiation.* Journal of Pharmaceutical Research International, 2014: p. 1341-1363.
3. Singh, A.P., et al., *Targeted therapy in chronic diseases using nanomaterial-based drug delivery vehicles.* Signal transduction and targeted therapy, 2019. 4(1): p. 1-21.
4. Díaz-García, D., et al., *Preparation and study of the antibacterial applications and oxidative stress induction of copper maleamate-functionalized mesoporous silica nanoparticles.* Pharmaceutics, 2019. 11(1): p. 30.
5. Wong, C.W., et al., *Response surface methodology optimization of mono-dispersed MgO nanoparticles fabricated by ultrasonic-assisted sol–gel method for outstanding antimicrobial and anti-biofilm activities.* Journal of Cluster Science, 2020. 31(2): p. 367-389.
6. Elkhenany, H., et al., *Comparison of different uncoated and starch-coated superparamagnetic iron oxide nanoparticles: implications for stem cell tracking.* International journal of biological macromolecules, 2020. 143: p. 763-774.
7. Abd Elkodous, M., et al., *Fabrication of Ultra-Pure Anisotropic Zinc Oxide Nanoparticles via Simple and Cost-Effective Route: Implications for UTI and EAC Medications.* Biological trace element research, 2020. 196: p. 297-317.
8. Abd Elkodous, M., et al., *Engineered nanomaterials as potential candidates for HIV treatment: Between opportunities and challenges.* Journal of Cluster Science, 2019. 30(3): p. 531-540.
9. Kluchova, K., et al., *Superparamagnetic maghemite nanoparticles from solid-state synthesis–Their functionalization towards peroral MRI contrast agent and magnetic carrier for trypsin immobilization.* Biomaterials, 2009. 30(15): p. 2855-2863.
10. Nehra, P., et al., *Antibacterial and antifungal activity of chitosan coated iron oxide nanoparticles.* British journal of biomedical science, 2018. 75(1): p. 13-18.
11. Su, C., *Environmental implications and applications of engineered nanoscale magnetite and its hybrid nanocomposites: A review of recent literature.* Journal of hazardous materials, 2017. 322: p. 48-84.
12. Park, Y.-H., et al., *Effect of the size and surface charge of silica nanoparticles on cutaneous toxicity.* Molecular & Cellular Toxicology, 2013. 9(1): p. 67-74.
13. Li, Q., et al., *Correlation between particle size/domain structure and magnetic properties of highly crystalline Fe 3 O 4 nanoparticles.* Scientific reports, 2017. 7(1): p. 1-7.
14. Nejadshafiee, V., et al., *Magnetic bio-metal–organic framework nanocomposites decorated with folic acid conjugated chitosan as a promising biocompatible targeted theranostic system for cancer treatment.* Materials Science and Engineering: C, 2019. 99: p. 805-815.
15. Frimpong, R.A. and J.Z. Hilt, *Magnetic nanoparticles in biomedicine: synthesis, functionalization and applications.* Nanomedicine, 2010. 5(9): p. 1401-1414.
16. Gupta, A.K., et al., *Recent advances on surface engineering of magnetic iron oxide nanoparticles and their biomedical applications.* 2007.
17. Gupta, A.K. and M. Gupta, *Synthesis and surface engineering of iron oxide nanoparticles for biomedical applications.* biomaterials, 2005. 26(18): p. 3995-4021.
18. Unsoy, G., et al., *Synthesis optimization and characterization of chitosan-coated iron oxide nanoparticles produced for biomedical applications.* Journal of Nanoparticle Research, 2012. 14(11): p. 964.
19. Zhang, Y., H.F. Chan, and K.W. Leong, *Advanced materials and processing for drug delivery: the past and the future.* Advanced drug delivery reviews, 2013. 65(1): p. 104-120.
20. Verma, M., K. Singh, and M.S. Bakshi, *Surface active magnetic iron oxide nanoparticles for extracting metal nanoparticles across an aqueous–organic interface.* Journal of Materials Chemistry C, 2019. 7(34): p. 10623-10634.
21. Nam, J., et al., *Surface engineering of inorganic nanoparticles for imaging and therapy.* Advanced drug delivery reviews, 2013. 65(5): p. 622-648.
22. Hotze, E.M., T. Phenrat, and G.V. Lowry, *Nanoparticle aggregation: challenges to understanding transport and reactivity in the environment.* Journal of environmental quality, 2010. 39(6): p. 1909-1924.
23. Schladt, T.D., et al., *Synthesis and bio-functionalization of magnetic nanoparticles for medical diagnosis and treatment.* Dalton Transactions, 2011. 40(24): p. 6315-6343.
24. Bakshi, P.S., et al., *Chitosan as an environment friendly biomaterial–a review on recent modifications and applications.* International journal of biological macromolecules, 2020. 150: p. 1072-1083.
25. Kumar, S., et al., *Chitosan nanocomposite coatings for food, paints, and water treatment applications.* Applied Sciences, 2019. 9(12): p. 2409.
26. Ngah, W.W., L. Teong, and M. Hanafiah, *Adsorption of dyes and heavy metal ions by chitosan composites: A review.* Carbohydrate polymers, 2011. 83(4): p. 1446-1456.
27. Shrifian-Esfahni, A., et al., *Chitosan-modified superparamgnetic iron oxide nanoparticles: design, fabrication, characterization and antibacterial activity.* Chemik, 2015. 69(1): p. 19-32.
28. Bradbury, R.S., et al., *Antimicrobial susceptibility testing of cystic fibrosis and non-cystic fibrosis clinical isolates of Pseudomonas aeruginosa: a comparison of three methods.* British journal of biomedical science, 2011. 68(1): p. 1-4.
29. Saxena, S. and C. Gomber, *Comparative in vitro antimicrobial procedural efficacy for susceptibility of Staphylococcus aureus, Escherichia coli and Pseudomonas species to chloramphenicol,*

ciprofloxacin and cefaclor. British journal of biomedical science, 2008. 65(4): p. 178-183.
30. Nobile, C.J. and A.D. Johnson, *Candida albicans biofilms and human disease.* Annual review of microbiology, 2015. 69: p. 71-92.
31. Manikandan, C. and A. Amsath, *Antibiotic susceptibility pattern of Escherichia coli isolated from urine samples in Pattukkottai, Tamilnadu.* Int. J. Curr. Microbiol. App. Sci, 2014. 3(10): p. 449-457.
32. Yoon, J.E., et al., *Antibiotic susceptibility and imaging findings of the causative microorganisms responsible for acute urinary tract infection in children: a five-year single center study.* Korean journal of pediatrics, 2011. 54(2): p. 79.
33. Habib, S., *Highlights for management of a child with a urinary tract infection.* International journal of pediatrics, 2012. 2012.
34. Campbell, M.M. and G. Johnson, *Chloramine T and related N-halogeno-N-metallo reagents.* Chemical Reviews, 1978. 78(1): p. 65-79.
35. Goehring, R.R., *Chloramine.* Encyclopedia of Reagents for Organic Synthesis, 2001.
36. Roorda, B.M., H.L. Nienhuis, and M.L. Schuttelaar, *Anaphylactic reaction caused by skin contact with the disinfectant chloramine-T.* Contact dermatitis, 2019. 80(5): p. 321-322.
37. Kanerva, L., et al., *Occupational allergic contact urticaria from chloramine-T solution.* Contact Dermatitis, 1997. 37(4): p. 180-181.
38. Blomqvist, A., et al., *Atopic allergy to chloramine-T and the demonstration of specific IgE antibodies by the radioallergosorbent test.* International archives of occupational and environmental health, 1991. 63(5): p. 363-365.
39. Pham, X.N., et al., *Synthesis and characterization of chitosan-coated magnetite nanoparticles and their application in curcumin drug delivery.* Advances in Natural Sciences: Nanoscience and Nanotechnology, 2016. 7(4): p. 045010.
40. Zavvar Mousavi, H. and S. Seyedi, *Kinetic and equilibrium studies on the removal of Pb (II) from aqueous solution using nettle ash.* Journal of the Chilean Chemical Society, 2010. 55(3): p. 307-311.
41. El-Batal, A.I., et al., *Response surface methodology optimization of melanin production by Streptomyces cyaneus and synthesis of copper oxide nanoparticles using gamma radiation.* Journal of Cluster Science, 2017. 28(3): p. 1083-1112.
42. Baraka, A., et al., *Synthesis of silver nanoparticles using natural pigments extracted from Alfalfa leaves and its use for antimicrobial activity.* Chemical Papers, 2017. 71(11): p. 2271-2281.
43. El-Batal, A.I., et al., *Biogenic synthesis of copper nanoparticles by natural polysaccharides and Pleurotus ostreatus fermented fenugreek using gamma rays with antioxidant and antimicrobial potential towards some wound pathogens.* Microbial pathogenesis, 2018. 118: p. 159-169.
44. El-Batal, A.I., et al., *Antimicrobial, antioxidant and anticancer activities of zinc nanoparticles prepared by natural polysaccharides and gamma radiation.* International journal of biological macromolecules, 2018. 107: p. 2298-2311.
45. Balouiri, M., M. Sadiki, and S.K. Ibnsouda, *Methods for in vitro evaluating antimicrobial activity: A review.* Journal of pharmaceutical analysis, 2016. 6(2): p. 71-79.
46. El-Batal, A.I., et al., *Antibiofilm and antimicrobial activities of silver boron nanoparticles synthesized by PVP polymer and gamma rays against urinary tract pathogens.* Journal of Cluster Science, 2019. 30(4): p. 947-964.
47. Mosallam, F.M., et al., *Biomolecules-mediated synthesis of selenium nanoparticles using Aspergillus oryzae fermented Lupin extract and gamma radiation for hindering the growth of some multidrug-resistant bacteria and pathogenic fungi.* Microbial pathogenesis, 2018. 122: p. 108-116.
48. Attia, M.S., et al., *Spirulina platensis-Polysaccharides Promoted Green Silver Nanoparticles Production Using Gamma Radiation to Suppress the Expansion of Pear Fire Blight-Producing Erwinia amylovora.* Journal of Cluster Science, 2019. 30(4): p. 919-935.
49. El-Sayyad, G.S., et al., *Facile biosynthesis of tellurium dioxide nanoparticles by Streptomyces cyaneus melanin pigment and gamma radiation for repressing some Aspergillus pathogens and bacterial wound cultures.* Journal of Cluster Science, 2020. 31(1): p. 147-159.
50. Abd Elkodous, M., et al., *Therapeutic and diagnostic potential of nanomaterials for enhanced biomedical applications.* Colloids and Surfaces B: Biointerfaces, 2019. 180: p. 411-428.
51. Brownlee, K., *Probit Analysis: A Statistical Treatment of the Sigmoid Response Curve*. 1952, JSTOR.
52. Amoli Diva, M. and K. Pourghazi, *Magnetic nanoparticles grafted pH-responsive poly (methacrylic acid-co-acrylic acid)-grafted polyvinylpyrrolidone as a nano-carrier for oral controlled delivery of atorvastatin.* Nanomedicine Research Journal, 2017. 2(1): p. 18-27.
53. Stoia, M., R. Istratie, and C. Păcurariu, *Investigation of magnetite nanoparticles stability in air by thermal analysis and FTIR spectroscopy.* Journal of Thermal Analysis and Calorimetry, 2016. 125(3): p. 1185-1198.
54. Kataria, N. and V. Garg, *Green synthesis of Fe3O4 nanoparticles loaded sawdust carbon for cadmium (II) removal from water: regeneration and mechanism.* Chemosphere, 2018. 208: p. 818-828.
55. Tang, Z.-X. and B.-F. Lv, *MgO nanoparticles as antibacterial agent: preparation and activity.* Brazilian Journal of Chemical Engineering, 2014. 31(3): p. 591-601.
56. Ashour, A., et al., *Antimicrobial activity of metal-substituted cobalt ferrite nanoparticles synthesized by sol–gel technique.* Particuology, 2018. 40: p. 141-151.
57. Maksoud, M.A., et al., *Antibacterial, antibiofilm, and photocatalytic activities of metals-substituted spinel cobalt ferrite nanoparticles.* Microbial pathogenesis, 2019. 127: p. 144-158.
58. El-Sayyad, G.S., et al., *Merits of photocatalytic and antimicrobial applications of gamma-irradiated $Co_xNi_{1-x}Fe_2O_4/SiO_2/TiO_2$; x= 0.9 nanocomposite for pyridine removal and pathogenic bacteria/fungi disinfection: implication for wastewater treatment*. RSC Advances, 2020. 10(9): p. 5241-5259.
59. Pal, S., Y.K. Tak, and J.M. Song, *Does the antibacterial activity of silver nanoparticles depend on the shape of the nanoparticle? A study of the gram-negative bacterium Escherichia coli.* Applied and environmental microbiology, 2007. 73(6): p. 1712-1720.
60. Ma, S., et al., *Responses of the Microbial Community Structure in Fe (II)-Bearing Sediments to Oxygenation: The Role of Reactive Oxygen Species.* ACS Earth and Space Chemistry, 2019. 3(5): p. 738-747.
61. El-Batal, A.I., et al., *Nystatin-mediated bismuth oxide nano-drug synthesis using gamma rays for increasing the antimicrobial and antibiofilm activities against some pathogenic bacteria and Candida species.* RSC Advances, 2020. 10(16): p. 9274-9289.
62. Hezma, A., A. Rajeh, and M.A. Mannaa, *An insight into the effect of zinc oxide nanoparticles on the structural, thermal, mechanical properties and antimicrobial activity of Cs/PVA composite.* Colloids and Surfaces A: Physicochemical and Engineering Aspects, 2019. 581: p. 123821.
63. El-Sayyad, G.S., et al., *Gentamicin-Assisted Mycogenic Selenium Nanoparticles Synthesized Under Gamma Irradiation for Robust Reluctance of Resistant Urinary Tract Infection-Causing Pathogens.* Biological Trace Element Research, 2020. 195: p. 323-342.
64. El-Batal, A.I., F.M. Mosallam, and G.S. El-Sayyad, *Synthesis of Metallic Silver Nanoparticles by Fluconazole Drug and Gamma*

Rays to Inhibit the Growth of Multidrug-Resistant Microbes. Journal of Cluster Science, 2018. 29(6): p. 1003-1015.
65. Matei, E., et al., *Leaching tests for synthesized magnetite nanoparticles used as adsorbent for metal ions from liquid solutions.* Digest Journal of Nanomaterials and Biostructures, 2011. 6(4): p. 1701-1708.
66. Chiou, M.-S., P.-Y. Ho, and H.-Y. Li, *Adsorption of anionic dyes in acid solutions using chemically cross-linked chitosan beads.* Dyes and pigments, 2004. 60(1): p. 69-84.
67. Wahab, H.S. and A.A. Hussain, *Photocatalytic oxidation of phenol red onto nanocrystalline TiO 2 particles.* Journal of Nanostructure in Chemistry, 2016. 6(3): p. 261-274.
68. Ollis, D.F., *Kinetics of photocatalyzed reactions: Five lessons learned.* Frontiers in chemistry, 2018. 6: p. 378.
69. Abd Elkodous, M., et al., *Carbon-dot-loaded* $Co_x Ni_{1-x} Fe_2 O_4$*;* $x = 0.9/SiO_2/TiO_2$ *nanocomposite with enhanced photocatalytic and antimicrobial potential: An engineered nanocomposite for wastewater treatment*. Scientific Reports, 2020. 10(1): p. 11534.
70. Abdel Maksoud, M.I.A., et al., *Nanostructured Mg substituted Mn-Zn ferrites: A magnetic recyclable catalyst for outstanding photocatalytic and antimicrobial potentials.* Journal of Hazardous Materials, 2020. 399: p. 123000.